Journal of Alloys and Compounds 1027 (2025) 180507

Contents lists available at ScienceDirect

Journal of Alloys and Compounds

journal homepage: www.elsevier.com/locate/jalcom

Acoustic emission during Lüders-band type martensitic transformation and thermal recovery in $Cr_{20}Mn_{20}Fe_{20}Co_{34.4}Ni_{5.6}$ high entropy shape memory single crystals

A. Azim Asmaa [a,b], Daróczi Lajos [a], Z.Tóth László [a], V. Kireeva Irina [c], I. Chumljakov Yuriy [c], L. Beke Dezső [a,*]

[a] Department of Solid State Physics, Doctoral School of Physics, University of Debrecen, P.O. Box 2, Debrecen H-4010, Hungary
[b] Physics Department, Faculty of Science Ain Shams University, Abbassia, Cairo 11566, Egypt
[c] Siberian Physical Technical Institute, Tomsk State University, Tomsk 634050, Russia

ARTICLE INFO

Keywords:
Shape memory
High entropy alloy
Stress induced martensitic transformation
Lüders-band
Burst-like thermal recovery
Acoustic emission

ABSTRACT

Acoustic emission, AE, during Lüders band type martensitic transformation and during thermal recovery in $Cr_{20}Mn_{20}Fe_{20}Co_{34.4}Ni_{5.6}$ (at%) high entropy shape memory single crystals are investigated. The stress induced Lüders-band type martensitic transformation was induced by application of uniaxial tensile stress along the $[\bar{1}44]$ direction at room temperature. It is shown that the Lüders-type martensite nucleation and propagation is an intermittent process and results in acoustic emission signals. There is large AE activity at the band localization and it gradually decreases during its propagation, which is also a jerky process. The large acoustic activity at the band localization is due to the presence of nucleation barrier of elastic origin, which is proportional to the Lüders-peak area. Sub-cycles of the propagation stage showed AE activity in accordance with the Kaiser effect. It is concluded, from the local equilibrium model of thermoelastic martensitic transformations, that the martensite formed during stress loading is stabilized by a large dissipative energy. The cumulative elastic energy gradually decreased during thermal recovery indicating that this process has also the intermittent character. Characteristic exponents of the acoustic emission signals obtained during Lüders-type transformation and thermal recovery are the same within the error bars and agree well with data obtained during stress or temperature induced martensitic transformations in $Ni_{49}Fe_{18}Ga_{27}Co_{6}$ shape memory single crystals.

1. Introduction

There is well-known evidence that stress induced martensitic transformations in polycrystalline NiTi shape memory alloys can take place under tension by localized phase transformation, i.e. the phase transformations exhibit localization and propagation of deformation in macroscopic shear bands (Lüders-like phase transformation) [1–5]. Similar behaviour has also been observed in other polycrystalline shape memory alloys (Ti-25Nb [6], FeMnNiAl [7]) or in single crystalline samples such as $Ni_{43}Fe_{18}Ga_{27}Co_{12}$ [8], NiFeGa [9], CuZnAl [10], or in CrMnFeCoNi high-entropy shape memory alloy [11]. These observations, besides providing new evidence to the understanding of the above Lüders-like phase transformation, are also important in achieving large or even giant shape memory effect [11] and very small or nearly zero hysteresis [8].

Regarding the nucleation and propagation of the above Lüders-bands (L-bands), there are observations (see e.g. [4,5,12]) that the band initiation (with stress drop) occurs in burst manner and with orders of magnitude higher local strain rate than the global strain rate. After its formation the L-band propagates with the global strain rate [4,5] and sometimes serrations on the stress-strain curve can also appear [1,5,8,12]. These facts suggest that the nucleation and propagation are not a smooth process but can have a jerky character and acoustic emission (AE) measurements, being fingerprints of local sudden strain changes [13], can provide important contribution to the understanding of the microscopic mechanisms. As it is emphasized in very recent models of Lüders-type martensitic transformations [4,5] they clearly represent a different microscopic mechanism than the dislocation related Lüders-deformations. Nevertheless, based on the similarity of the loading stress-strain curves (mechanical instability, stress-drop at the

---

[*] Corresponding author.
E-mail address: dbeke@science.unideb.hu (L.B. Dezső).

https://doi.org/10.1016/j.jallcom.2025.180507
Received 19 February 2025; Received in revised form 28 March 2025; Accepted 17 April 2025

localization of the band followed by a stress plateau, zero or negative effective modulus in the plateau region [5,14]) in some phenomenological simulations such similarities can be used to describe the macroscopic features (see e.g. [14]). It is worth adding that as compared to numerous papers devoted to investigation of AE during classical L-band propagation by dislocation assisted plastic deformation [15–23], there is a lack of similar, detailed investigations on AE during Lüders-like phase transformations (see [24] and [25] as exceptions in polycrystalline NiTi). Regarding high entropy shape memory alloys, while there is a paper on AE investigation of the details of the plastic deformation mechanism of $Fe_{40}Mn_{40}Co_{10}Cr_{10}$(at%) [26], there are no publications on AE investigations of martensitic transformation in general and thus on AE investigations of Lüders-band type martensitic transformation. These alloys have unique properties [26–29], including high strength, high temperature superelasticity and martensitic transformation temperatures as well as excellent thermal cycling stability. In [28] the design of the $Cr_{20}Mn_{20}Fe_{20}Co_{40-x}Ni_x$ for shape memory applications was implemented and on the basis of this it was shown in [11] that these single crystals along a special orientation can indeed show giant shape memory effect.

In this article we provide results on acoustic emission measurements during Lüders-band like superelastic transformation under tensile stress in $Cr_{20.57}$ $Mn_{19.81}$ $Fe_{19.75}$ $Co_{34.31}$ $Ni_{5.56}$ (at%) high entropy (HEA) shape memory single crystals. It was shown, for the first time, in [11] that in these single crystals a tensile stress induced FCC→HCP martensitic transformation along $[\bar{1}44]$ direction took place with giant shape memory effect 15.7 ± 0.2 % (which is 90 % of the attainable maximum value) at $M_s = 195\ K$. After the transformation to martensite by Lüders-band nucleation and propagation, the sample remained in martensitic state after removing the stress and a burst-like recovery to the austenitic state was observed upon heating at about 400 K. It was also noted in [11] that the Lüders band deformation was completely reversible upon heating. The above behaviour offers investigation of both the Lüders-like transformation and burst-like thermal recovery by AE measurements, implemented in this work for the first time.

2. Experimental

Single crystals $Cr_{20.57}Mn_{19.81}Fe_{19.75}Co_{34.31}Ni_{5.56}$ (at%) HEAs were grown by the Bridgman method at a rate of 0.8 mm/min in alumina (Al_2O_3) crucibles and helium atmosphere at Tomsk University, Russia. The melting temperature is about 1820 K. We used two samples each having a dog-bone shaped, oriented along the $[\bar{1}44]$ tensile direction and with the {110} surface plane. The as-grown sample was cut into two pieces using electrical discharge machining (wire-erosion). Sample A has a gauge length of 10 mm and a cross section of $2.5 \times 0.4\ mm^2$, while sample B has a gauge length of 10 mm and a cross section of $2.5 \times 0.3\ mm^2$. Homogenization of the samples was carried out at 1473 K for 48 hours under Helium atmosphere, followed by water quenching. Since in our measurements we used the same samples as investigated in [11], where the microstructural characterization of them was also made, we concentrate here on the AE investigation of Lüders-band type martensitic transformation and on the reverse transformation during thermal recovery.

Tensile measurements were carried out using Instron tensile machine (No. 4465) at strain rate $7 \times 10^{-4}\ s^{-1}$ at room temperature. During the tensile experiments simultaneous acoustic emission (AE) measurements were carried out. For AE measurements, two piezoelectric sensors MICRO-100S and MICRO (Physical Acoustic Corporation, Princeton junction, NJ, USA) were used. The two sensors (microphones) had frequency response between 30 KHz and 1 MHz, and the response is nearly flat in the range of 0.2 MHz to 1 MHz (at about ∼ 75 dB in average) with maximum ± 10 dB deviation (1 V reference value). For the data acquisition, Sensophone Acoustic Emission Diagnostic (AED404) device (Geréb és Társa Kft, Hungary) was used. The data acquisition was performed by collecting of "hit mode" signals, where an analogue to digital converter was used with sampling rate 16 MHz and band-pass in the range of 30 KHz to 1 MHz. The collection of signals was made above a fixed threshold level: 36 dB. A 30 dB preamplifier, and a main logarithmic gain amplifier with 90 dB dynamic range were used.

The acoustic avalanches parameters (amplitude A, area S, and energy E) were calculated from the detected voltage $U(\mathrm{t})$ (temporal avalanche shape), where A is the maximum value of the voltage, $S = \int_0^D |U(t)|dt$, and $E = \frac{1}{R}\int_0^D U^2(t)dt$ (R is an arbitrarily chosen resistance ($\mathrm{R} = 1\mathrm{M\Omega}$)) and D is the duration time of the avalanche.

Sample A was loaded by tensile stress along the $[\bar{1}44]$ direction at room temperature up to 9 % strain. At about 120 MPa, a Lüders-band has been nucleated and propagated leading to a mixture of martensite and remaining austenite state (see Fig. 3b in [11]: the full transformation to martensite happens at about 14 % strain). Then, the recovery to the austenite phase was initiated by heating the sample. During the stress induced martensitic transformation and during the reverse thermal recovery we simultaneously measured the acoustic emission.

Several experimental cycles (typically 6, 4, and 2 cycles) up to 8 % strain were made on Sample B. Before making any new cycle, we heated the sample in argon environment for 15 min at 593 K, as it was recommended in [11]. For each cycle, we measured the acoustic emission simultaneously. This, after the removal of the load, was followed by heating for thermal recovery (again with simultaneous measurement of the acoustic emission) in the temperature range between 303 K and 473 K with 10 K/min heating rate). For some cycles, in order to monitor the reverse transformation back to austenite, we measured the change in the sample length.

Another set of loading measurements, without thermal recovery, was carried out simultaneously with acoustic emission measurements by splitting the main stress-strain loop (up to 4 %) into sub-loops performing a series of 23 cycles of loading and unloading on the sample between about 0 and 120 MPa.

The jerky character of martensitic transformation leads to self-similar AE noises and the probability distribution density functions of AE signal parameters, x, follow a truncated power law [30–33]:

$$P(x) \propto x^{-\mu} \exp\left(-\frac{x}{x_c}\right), \tag{1}$$

where μ is the characteristic exponent and x_c is the cutoff value. Here x can denote the amplitude, A, area, S, or energy, E, or duration, D, of AE avalanches. Furthermore, well-known power law relations exist between the measured avalanche parameters. For instance, the mean field theory, MFT, [32–37] predicts that $S \sim D^{\gamma}$ with $\gamma = 2$ and $S \propto A^2$ as well as $E \propto A^3$. Thus, the probability density functions, PDF, will be calculated using logarithmic boxing of the quantities $P(x_i) \sim \frac{N_i}{N}$, where N_i and N denote the number of events at a certain value of x_i and the number of all hits, respectively. The PDFs will be fitted using a two parametrical nonlinear fitting by the Levenberg-Marquardt least squares method.

3. Results

3.1. Acoustic emission during Lüders-band nucleation and propagation

Fig. 1 shows the stress-strain curve (black) as well as the simultaneously measured amplitudes of AE signals (red) (a), together with the cumulative number of AE energy ($E_c = \sum_i E_i$) (green curve) as well as the AE activity (blue) (b), during deformation of samples up to 9 % with $7 \times 10^{-4}\ s^{-1}$ strain rate. It can be seen that there is a peak in the AE activity at the nucleation of the Lüders-band (at the maximum of the stress-strain curve) which is followed by a gradual decrease during the propagation of the band (Fig. 1b). The propagation stage contains still (decreasing number) discrete AE signals, most of which correlates well

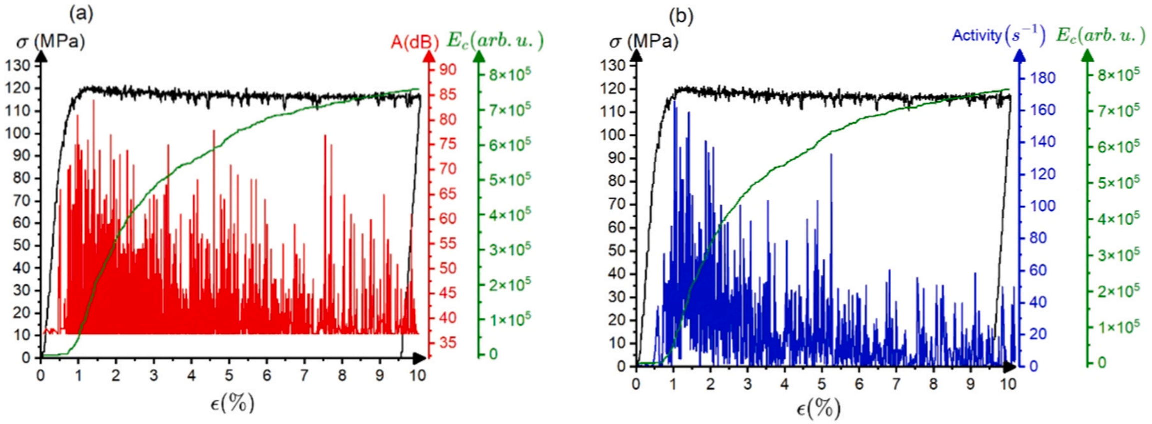

Fig. 1. Stress-strain curve (black) as well as the simultaneously measured amplitudes of AE signals (red) (a), together with the cumulative number of AE energy ($E_c = \sum_i E_i$) (green curve) as well as the AE activity (b) (blue), during deformation of samples up to $9^{\%}$ with 7×10^{-4} s^{-1} strain rate.

with local stress drops. Indeed, as it can be seen in Fig. 2, almost all large stress drops correlate well with AE signals.

3.2. Acoustic emission results during thermal recovery

Fig. 3 shows the macroscopic length change of the sample, the AE activity and the cumulative acoustic energy during thermal recovery (after transformation up to 8 % strain). The martensite to austenite transformation takes place in a 70 K wide temperature interval, within which there is a well measurable AE activity. The cumulative AE energy gradually (in a stepwise manner) increases and the maximum of the activity and the largest vertical jump in E_c appear at around the inflexion point of the length change curve.

3.3. Characteristic AE exponents for Lüders-type transformation

As an illustration, Figs. 4 and 5 show the energy and area distributions of AE avalanches measured during stress induced Lüders-type martensitic transformation (sample A). It can be seen that straight lines can be fitted very well over about three-six orders of magnitude to the PDF functions. The maximum likelihood fit is a recommended method to check the reliability of exponents calculated from the log P versus log E plots [38]. We obtained that in all cases the exponents determined by the two methods were the same, within the error bars given in Table 1 (see also Figs. 4a and 4b). Table 1 shows the calculated exponents for energy, amplitude, and area.

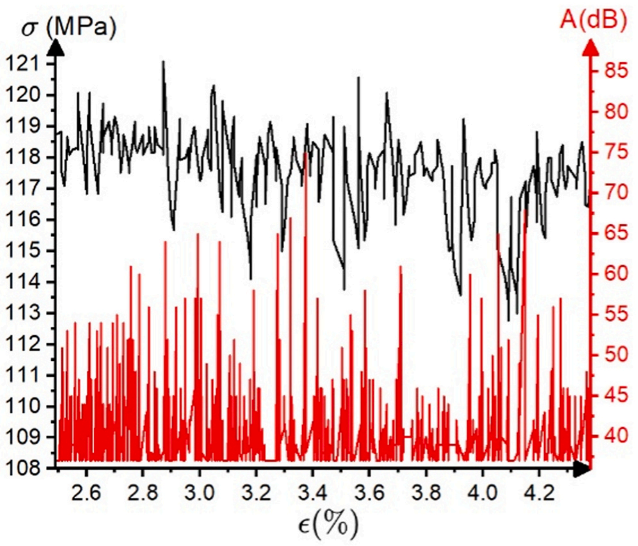

Fig. 2. Enlarged part of the propagation stage between 2.5 % and 4.3 % strain (see also Fig. 1a).

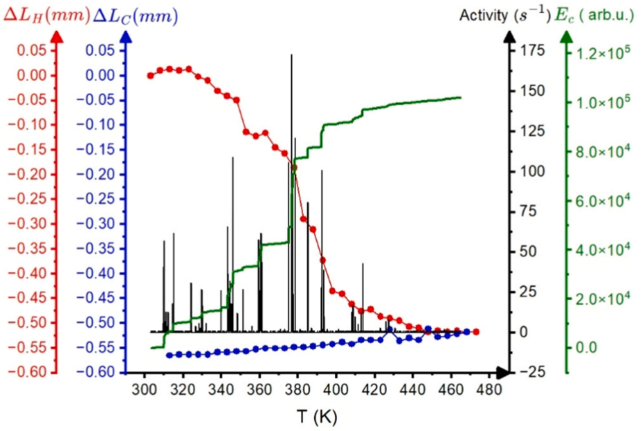

Fig. 3. Macroscopic length change of the sample (red and blue dots for heating and cooling, respectively), the AE activity (black lines) and the cumulative acoustic energy (green curve) during thermal recovery (after the deformation cycle up to 8 % strain).

Figs. 6 and 7 show the power relations between the area, *S*, and amplitude, *A*, as well as energy, *E*, and amplitude, *A,* respectively. In Figs. 6a and 7a all the measured points are shown, while in Figs. 6b and 7b show the data after logarithmic boxing: the points represent the values averaged within a certain logarithmic box. The latter plotting is used in order to get a more realistic estimate for the characteristic exponents. In Table 1 the values of φ are given: φ is the parameter present in the characteristic exponents; $S \propto A^{2-\varphi}$ as well as $E \propto A^{3-\varphi}$ and characterizes the deviation from the values predicted by the mean field theory: large φ values (close to unity) mean "enigma of acoustic emission" [37,39] (see also the discussion).

3.4. Characteristic AE exponents for thermal recovery

Figs. 8 and 9, show, as an illustration, the energy and area distributions of AE avalanches measured during thermal recovery after stress induced transformation up to 8 % strain. The number of AE events detected during one cycle were relatively small and in order to increase the statistics we averaged the data points for 4 repeated heating cycles. It can be seen that the straight lines can be well fitted over about three orders of magnitude. The maximum likelihood fits provided the same

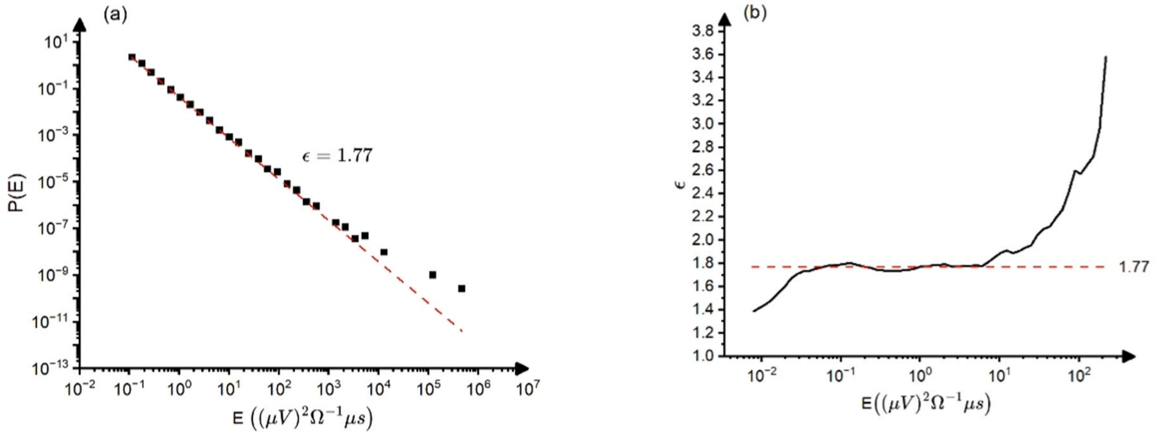

Fig. 4. Energy dirtibution function (a) and the correspoding maximum likelihood, ML, fit (b), for Lüders-band like transformation up to 9 % strain. It can be seen that the exponent of the fitted stright line and the value of the provided ML fit agrees with each other within an error bar ± 0.1 (see also Table 1).

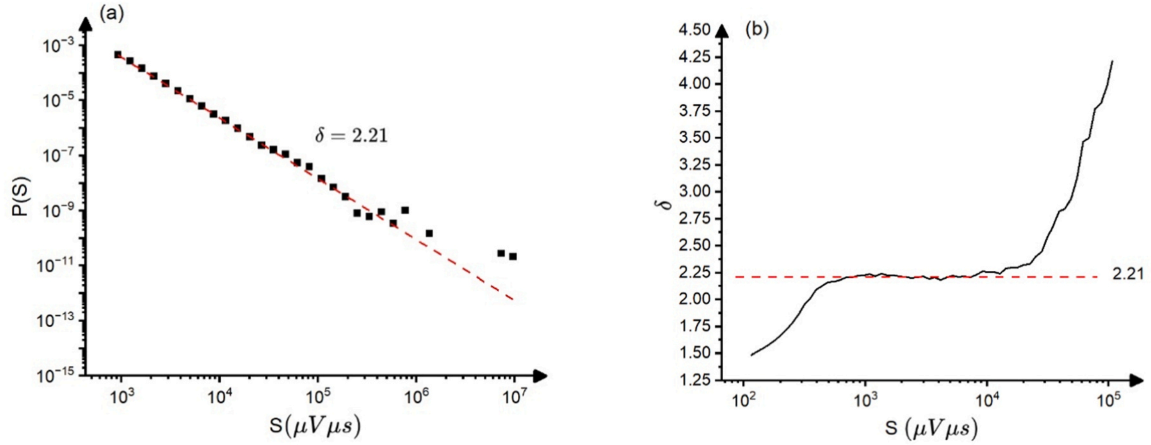

Fig. 5. Area distribution function (a) and the correspoding maximum likelihood, ML, fit (b),), for Lüder-band like transformation up to 9 % strain. It can be seen that the exponent of the fitted straight line and the value of the provided ML fit agrees with each other within an error bar ± 0.1 (see also Table 1).

Table 1
Characteristic exponents for Lüders-type martensitic transformation.

P(E) ~ $E^{-\varepsilon}$ ε	P(A) ~ $A^{-\alpha}$ α	P(S) ~ $S^{-\delta}$ δ	$E \sim A^{3-\varphi}$ φ	$S \sim A^{2-\varphi}$ φ
1.8±0.1	2.7±0.2	2.2 ±0.1	0.6 ± 0.2	0.4 ± 0.2

exponents within the error bars given in Table 2.

Figs. 10 and 11 show the power relations between the area, S, and amplitude, A, as well as energy, E, and amplitude, A, respectively for thermal recovery. Similarly as above in Figs. 6 and 7 all the measured points are shown in Figs. 10a and 11a, while Figs. 10b and 11b shows the data after logarithmic boxing. Table 2 shows the calculated exponents for energy, amplitude and area and the exponents φ for thermal recovery.

4. Discussion

4.1. Lüders-type martensitic transformation

Figs. 1 and 2 nicely illustrate that the Lüders-type martensite nucleation and propagation is an intermittent process and results in acoustic emission signals. The large AE activity at the band localization and a gradual decrease of it during the propagation is in agreement with other observations on AE during plastic deformation [21,40]. It was concluded in [40] that there is a peak in the AE activity just at the nucleation of Lüders band, which is followed by a continuous decrease. The gradually decreasing slope of the cumulative energy in Fig. 1 is also a manifestation of the above trend. In addition to this, our Figs. 1 and 2 also illustrate that the propagation of the band is also a jerky process consisting of local stress drops, most of which is accompanied with AE (Fig. 2). In order to have a deeper insight into the details of the band propagation, Fig. 12 shows the results of AE measurements made simultaneously with successive local cycles of the stress-strain curve, splitting it into sub-loops performing 23 local cycles of the main loop (measured up to 4 %): the numbers denote the successive sub-loops. It can be seen that a) there is no AE activity during the first three sub-cycles (which were in the elastic regime) and b) in general in sub-cycles with lower top stress than the previous top value, there is practically no AE activity. The latter fact is the well-known Kaiser effect [41]: absence of AE signals until the stress reached the former highest level [41].

For the interpretation of the observed stress-strain curve and the features of thermal recovery it is useful to carry out thermodynamic analysis as proposed in [42]. We will use here the local equilibrium model [43], which is based on the condition that the derivative of the change of the Gibbs free energy by the transformed martensite volume fraction, ξ, should be zero. Thus, the lower branch (transformation from austenite, A, to martensite, M, indicated by the ↓ upper index) of the $T(\xi)$ or $\sigma(\xi)$ hysteresis loop (T and σ have their usual meaning) is obtained

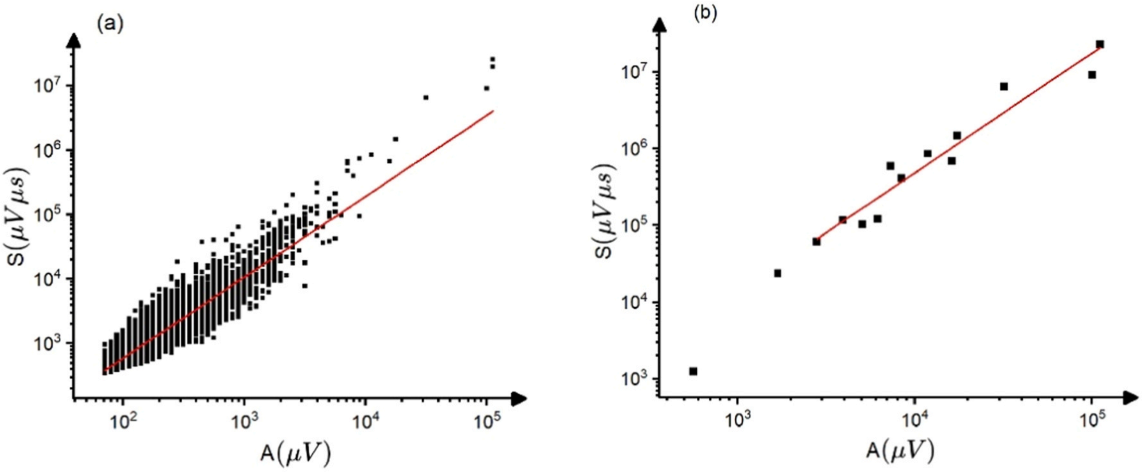

Fig. 6. *LogS* versus *logA*: a) all data points, (b) after logarithmic boxing, for Lüder-band like transformation up to 9 % strain. The slope in b) is 1.6.

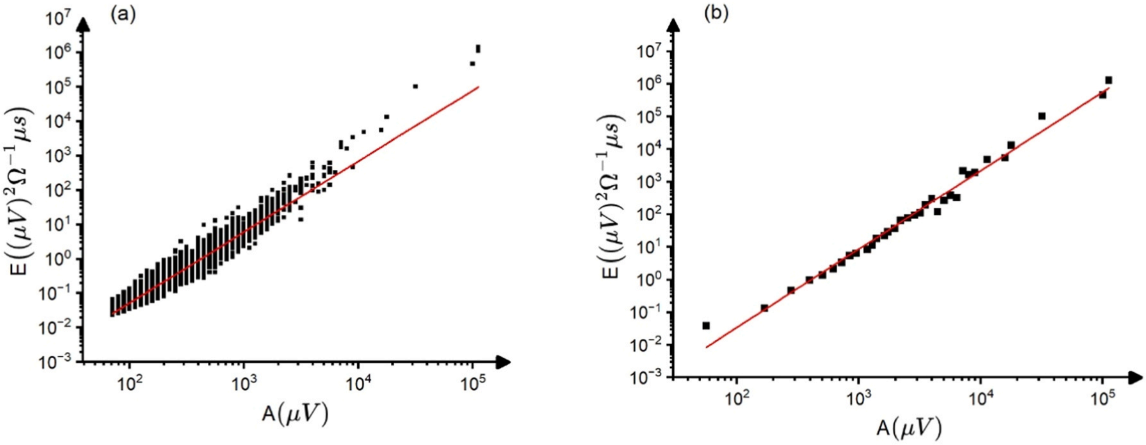

Fig. 7. *LogE* versus *logA*: a) all data points, (b) after logarithmic boxing, for Lüder-band like transformation up to 9 % strain. The slope in b) is 2.4.

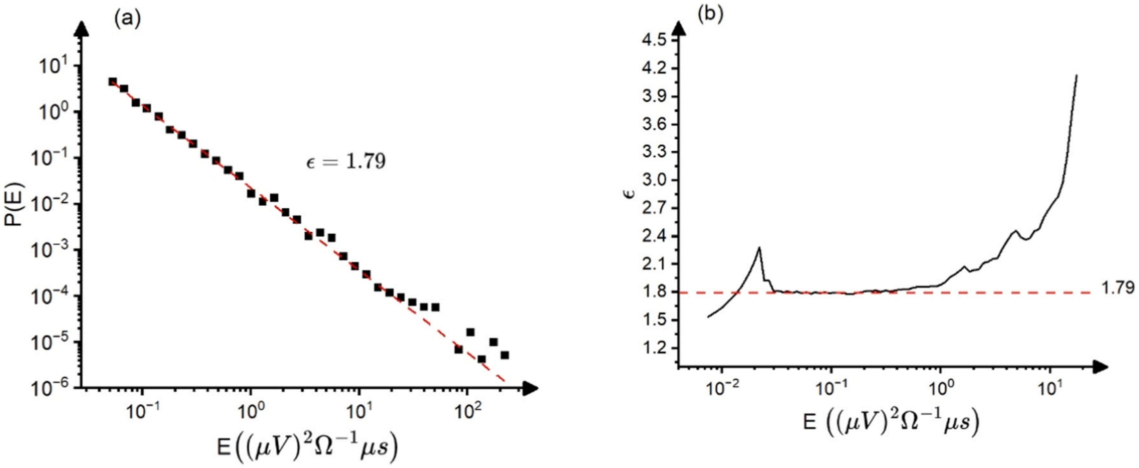

Fig. 8. Energy dirtibution function (a) and the correspoding maximum likelihood, ML, fit (b), for thermal recovery. It can be seen that the exponent of the fitted stright line and the value provided ML fit agree with each other within an error bar ± 0.1 (see also Table 2).

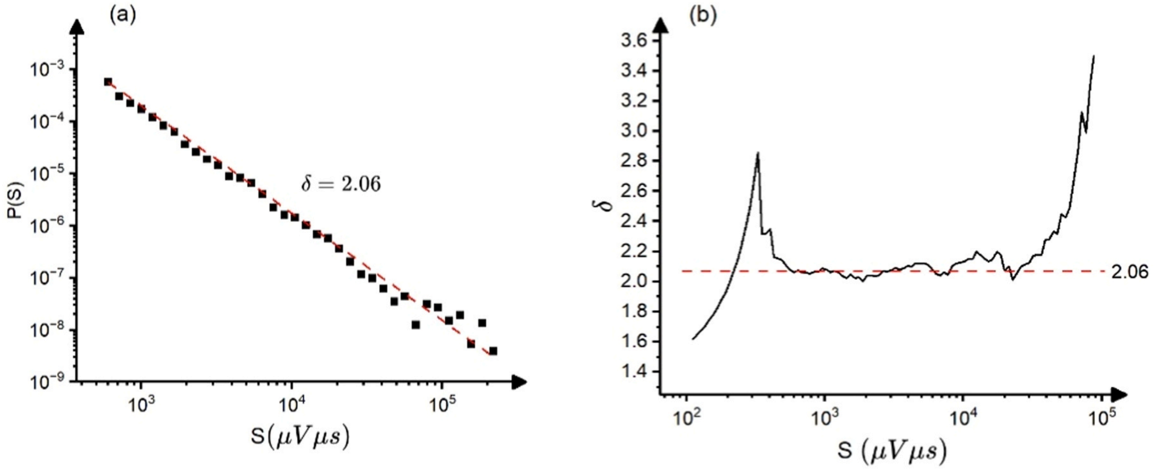

Fig. 9. Area distribution function (a) and the correspoding maximum likelihood, ML, fit (b), for thermal recovery. It can be seen that the exponent of the fitted stright line and the value provided ML fit agree with each other within an error bar ± 0.1 (see also Table 2).

Table 2
Characteristic exponents for thermal recovery.

P(E) ~ $E^{-\varepsilon}$ ε	P(A) ~ $A^{-\alpha}$ α	P(S) ~ $S^{-\delta}$ δ	$E \sim A^{3-\varphi}$ φ	$S \sim A^{2-\varphi}$ φ
1.8±0.1	2.7±0.2	2.1 ±0.1	0.6 ± 0.2	0.4 ± 0.2

from this condition, for zero hydrostatic pressure [43], as:

$$\frac{\partial \Delta G^{\downarrow}(\xi)}{\partial \xi} = 0 = \frac{\partial\left(\Delta G_c^{\downarrow} + D^{\downarrow} + E^{\downarrow}\right)}{\partial \xi} = \Delta g_c^{\downarrow} + d^{\downarrow}(\xi) + e^{\downarrow}(\xi) \tag{2}$$

where Here, $\Delta g_c^{\downarrow}$ is the difference of the chemical free energies of the pure M and A phases [1]

$$\begin{aligned}\Delta g_c^{\downarrow} &= \frac{\partial \Delta G_c^{\downarrow}}{\partial \xi} = \frac{\partial[\xi G_M + (1-\xi)G_A - G_A]}{\partial \xi} = G_M - G_A \\ &= u_M - u_A - T(s_M - s_A) - \sigma V \varepsilon^{tr} = \Delta u^{\downarrow} - T\Delta s^{\downarrow} - \sigma V \varepsilon^{tr\downarrow}\end{aligned} \tag{3}$$

V as well as $\varepsilon^{tr\downarrow}$ are the molar volume and the transformation strain, respectively. Furthermore, both $\Delta u^{\downarrow}$ and $\Delta s^{\downarrow}$ are negative and $d^{\uparrow}(\xi) = \frac{\partial D^{\uparrow}(\xi)}{\partial \xi}$ as well as $e^{\uparrow}(\xi) = \frac{\partial E^{\uparrow}(\xi)}{\partial \xi}$, with the dissipative and elastic energies of the $M \rightarrow A$ transformation ($D^{\downarrow}$ and $E^{\downarrow}$), respectively ($D^{\uparrow} \cong D^{\downarrow} > 0$ and $-E^{\uparrow} \cong E^{\downarrow} > 0$ for thermoelastic transformations [43]). Since the nucleation energy has the same sign as D in both directions, and thus it is not easily distinguishable from it, we can consider that the nucleation energy is included in D [43]. Similar equations can be written for the upper branch of the hysteresis loop with upper index ↑. From Eqs. (2) and (3) one get that the inverses of the lower and upper branches of the thermal hysteresis loops have the from

$$T^{\downarrow}(\xi) = T_o(\sigma) + \frac{d^{T\downarrow}(\xi) + e^{T\downarrow}(\xi)}{\Delta s^{\downarrow}}, \tag{4}$$

$$T^{\uparrow}(\xi) = T_o(\sigma) + \frac{d^{T\uparrow}(\xi) + e^{T\uparrow}(\xi)}{\Delta s^{\uparrow}}, \tag{5}$$

where T_o is the equilibrium transformation temperature ($T_o(\sigma) = \frac{\Delta u^{\downarrow}}{\Delta s^{\downarrow}} + \frac{\sigma V \varepsilon^{tr}}{\Delta s^{\downarrow}} = T_o(0) + \frac{\sigma V \varepsilon^{tr}}{\Delta s^{\downarrow}}$) and $\Delta u^{\uparrow} = -\Delta u^{\downarrow} > 0$ as well as $\Delta s^{\uparrow} = -\Delta s^{\downarrow} = -\Delta s > 0$. The d and e terms depend only on ξ at fixed values of σ, at which typically the thermal hysteresis loops are measured. Furthermore, it can also be assumed that the dissipative energy is proportional to ξ, i.e. $d^{T\uparrow}(\xi) = const.$, and is the same in both directions i.e. $d^{T\uparrow}(\xi = 0) = d_o^{T\uparrow} = d_1^{T\uparrow} = d^{T\uparrow}(\xi = 1)$ *and* $d_o^{T\downarrow} = d_1^{T\downarrow}$, as well as that $E^{\uparrow}$ has a quadratic dependence on ξ (due to overlap of the elastic fields of the nuclei of the second phase) [43]. Thus

$$e^{T\downarrow}(\xi) = e_o^{T\downarrow} + \left(e_1^{T\downarrow} - e_o^{T\downarrow}\right)\xi, \tag{6}$$

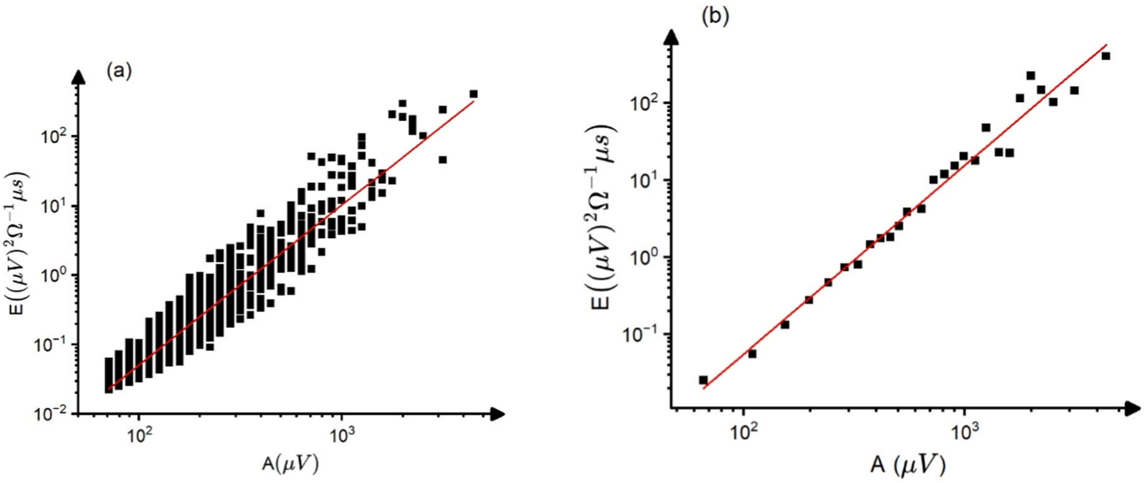

Fig. 10. *LogE* versus *logA*: a) all data points, (b) after logarithmic boxing for thermal recovery. The slope in b) is 2.4.

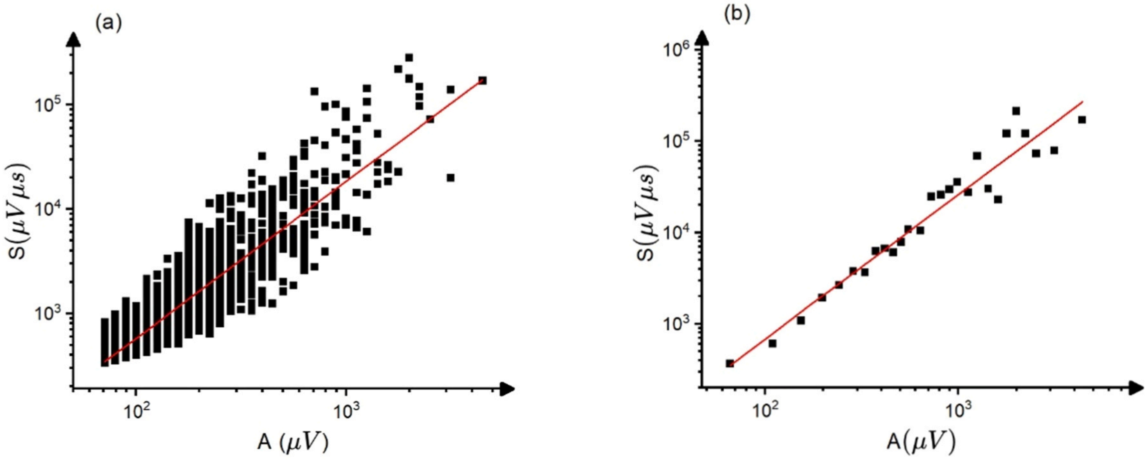

Fig. 11. *LogS* versus *logA*: a) all data points, (b) after logarithmic boxing for thermal recovery. The slope in b) is 1.6.

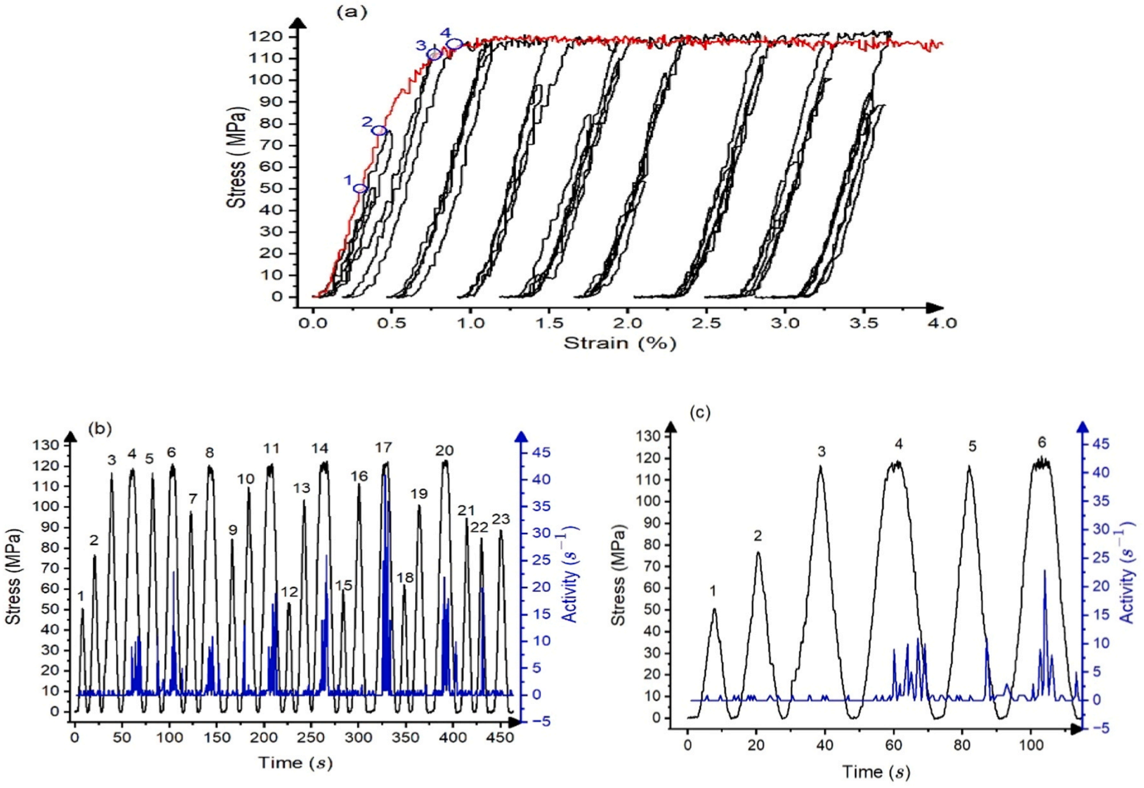

Fig. 12. AE result synchronized with the successive sub-loops on the main stress-strain curve (measured up to 4 %): a) the mains loop (red) and the successive sub-loops (black); b) Successive stress-strain loops (black curves) and the corresponding AE activity (blue); c) the same as b) but only for the first six sub-cycles.

and

$$e^{T\uparrow}(\xi) = e_o^{T\uparrow} - \left(e_1^{T\uparrow} - e_o^{T\uparrow}\right)\xi. \tag{7}$$

Note

$$E^{T\downarrow} = \int_0^1 e^{T\downarrow}(\xi)d\xi = \frac{e_o^{T\downarrow} + e_1^{T\downarrow}}{2}$$

and

$$E^{T\uparrow} = \int_0^1 e^{T\uparrow}(\xi)d\xi = \frac{e_o^{T\uparrow} + e_1^{T\uparrow}}{2}. \tag{8}$$

Similarly, from (2) and (3) expressions for the branches of the $\sigma(\xi)$ hysteresis loops, measured at fixed temperature during stress induced transformations, can be obtained [39] as

$$\sigma^{\downarrow}(\xi) = \sigma_o(T) + \frac{e^{\sigma\downarrow}(\xi) + d^{\sigma\downarrow}(\xi)}{V\varepsilon^{tr\downarrow}} \tag{9}$$

$$\sigma^{\uparrow}(\xi) = \sigma_o(T) + \frac{e^{\sigma\uparrow}(\xi) + d^{\sigma\uparrow}(\xi)}{V\varepsilon^{tr\uparrow}}. \tag{10}$$

Here $\varepsilon^{tr\downarrow} = -\varepsilon^{tr\downarrow}$ and for tensile stress induced $A\rightarrow M$ transformation $(\sigma > 0)$ during loading $\varepsilon^{tr\downarrow} > 0$ and during unloading $-\varepsilon^{tr\uparrow} < 0$ as well as $\sigma_o(T) = \sigma_o(0) - T\frac{\Delta s^{\downarrow}}{Ve^{tr}}$. Note the values of the d and e terms obviously can be different in experiments taken at fixed stress or temperature, respectively: this is expressed by the use of T and σ upper indexes.

Expressions giving the start and finish temperatures (M_s, M_f, A_s and A_f) or stresses (σ_{Ms}, σ_{Mf}, σ_{As}, σ_{Af}) of a given branch of the hysteresis loops can be simply obtained from (4) and (5) as well as from (9) and (10) by taking the d and e terms at $\xi = 0$ and $\xi = 1$, respectively [43].

Before the application of this model for the L-band formation/propagation and thermal recovery, let us summarize the thermodynamic parameters estimated from the start and finish temperatures of the "normal" thermal hysteresis loop, as well as from the Clausius-Clapeyron relation i.e. from the $\frac{d\sigma_{Ms}}{dT} = -\frac{\Delta s}{\varepsilon^{tr}} = \frac{0.6MPa}{K}$ slope from data published in [11]. Using that the molar volume of our alloy is 7×10^{-6} m^3/mol, $-\Delta s = \left(\frac{0.6MJ}{m^3K}\right) * 0.157 = 94\frac{kJ}{m^3K} = 0.66\frac{J}{molK}$ (for ε^{tr} 15.7 % was also taken form [11]). From the Table 2 of [11], we can write $W^{\uparrow} \cong W^{\downarrow} \cong 25K$ as well as $\Delta T = 165K$, i.e. using (4) we get from $W^{\downarrow} = M_s - M_f = \frac{e_1^{T\downarrow} - e_o^{T\downarrow}}{-\Delta s} = \frac{e_1^T - e_o^T}{-\Delta s}$ as well as from $\Delta T = \left(\frac{A_s + A_f}{2} - \frac{M_s + M_f}{2}\right) = \frac{1}{-\Delta s}\left[D^{T\uparrow} + D^{T\downarrow} + E^{T\uparrow} + E^{T\downarrow}\right]$ that

$$e_1^T - e_o^T = 25 * 0.66J = 16.5 \quad J/mol \tag{11}$$

as well as

$$D_T = 2D^T = \Delta T(-\Delta s) = 109\frac{J}{mol}, \tag{12}$$

respectively, where D_T is the dissipative energy of the whole thermal loop. In (12) it was also used that for thermoelastic transformations $E^{T\uparrow} + E^{T\downarrow} = 0$ and $D^{T\uparrow} + D^{T\uparrow} = 2D^T = 2d_o^{T\downarrow} = 2d_o^T$. Although in Table 2 of [11] $W^{\uparrow} = 40K$ as well as $W^{\downarrow} = 10K$ is given, in order to remain within the thermoelastic approximation (in which $W^{\uparrow} = W^{\downarrow}$) their arithmetic mean was taken. Thus, the error bar for 25 K is large (about 100 %): this choice is also supported by data given for alloy Ni3 in [11] where $W^{\uparrow} = W^{\downarrow}$ indeed fulfilled. Taking into account that $D^T = d_o^T = d_1^T$, from the value shown in (12), we get that $d_o^T = 55\frac{J}{mol}$. The large value of the dissipative energy indicates that in this alloy the motion of the A/M interface(s) is relatively difficult (due to interactions with dislocations and stacking faults: see also Fig. 5 of [11]).

Regarding the present experiments, let us consider first the stress-induced transformation by L-band formation. According to the Liu's concept [4,5], it is worth to make a distinction between the localization and propagation stage. In the nucleation stage we observed a maximum on the AE activity at around the small stress peak of the L-band formation. Let us assume, that in the nucleation of the L-band the elastic energy, related to the stress peak at the nucleation stage, dominates (and the energy for the creation of the austenite/martensite interface is less important). Then, according to [4,5] this nucleation energy should be the integral of the stress versus strain function from the beginning until the end of the band formation (see Fig. 4b in [5]) i.e. it is measured by the area below the stress peak. This can be approximated by the area of a triangle of σ_p height and ε_{Lend} wide (σ_P and ε_{Lend} are the maximum and width of the Lüders band peak after nucleation, but before its propagation). This gives (see also Fig. 1b)

$$D_N = \frac{1}{2}\sigma_P\varepsilon_{Lend} = \frac{1}{2}\sigma_P \quad 0.020 \cong 60(MPa) * 0.020 = 1.2\frac{MJ}{m^3} = 9 \quad \frac{J}{mol}. \tag{13}$$

This result also shows that D_N is smaller than D_T by about an order of magnitude, and has similar value as the slope of the first derivative of the elastic energy for thermally induced transformation.

Regarding the dissipative energy, D, in the band propagation stage we can again use that $D^\sigma = d_o^\sigma\xi$ and $D^{\sigma\uparrow} = D^{\sigma\downarrow} = D^\sigma$, i.e. $\frac{\partial D^\sigma}{\partial \xi} = d_o^\sigma = d_1^\sigma = const$. Furthermore, we can approximately write, using (4), for the almost horizontal stress strain curve (where now σ_{Ms} is taken at $\xi_{Lend} = \frac{l_{Lend}}{L_o} = \frac{\varepsilon_{Lend}}{\varepsilon^{tr}}$, from where the pure propagation started: we use notations of [4,5]: L_o is the gauge length) that

$$\sigma_{Mf} - \sigma_{Ms} = \frac{e_1^{\sigma\downarrow} - e_o^{\sigma\downarrow}}{V\varepsilon^{tr\downarrow}} \cong 0. \tag{14}$$

(In fact $\sigma_{Mf} - \sigma_{Ms}$ is about 2 MPa in our Fig. 1, i.e. it is not exactly zero, but corresponds to $e_1^{\sigma\downarrow} - e_o^{\sigma\downarrow} \cong$ 2J/mol, which can be neglected.) This is also in accordance with the model of [4,5], since in this stage $\sigma_{Mf} - \sigma_{Ms} = 0$. Similarly $\sigma_{As} = \sigma_{Af}$ is also expected. Note, that we can not get quantitative conclusion for the value of $e_o^{\sigma\downarrow}\left(= \frac{\partial E^{\downarrow}}{\partial \xi}{}_{at \xi = \xi_{Lend}}\right)$ from the loading σ-ε branch alone. But, from Fig. 4b of [3] on the $\xi(\varepsilon)$ dependence of σ, which can be considered as good model example for the ξ-dependence of the elastic energy during nucleation of L-band, we get a qualitative conclusion that it is negative and should be small. Since the elastic energy, in the $0 < \xi < \xi_{Lend} = \frac{\varepsilon_{Lend}}{\varepsilon^{tr}}$ interval, is proportional to $\frac{1}{2E}\sigma^2$ (E is the elastic modulus), and σ is a fast decaying function of $\frac{\varepsilon_{Lend}}{\varepsilon^{tr}}$ in Fig. 4b of [3], its derivative by ξ should be also very small negative value at about $\varepsilon_{Lend} = 1.2$ %, (i.e. at $\xi_{Lend} = \frac{\varepsilon_{Lend}}{\varepsilon^{tr}} = 0.076$).

Furthermore, since the transformed martensite (left behind the propagating L-band boundary) is stable (the sample remains in martensitic state after switching down the stress to zero at different stages), we can conclude that the $\sigma = 0$ stress is not enough for the backward transformation, even in the present of a small produced martensite volume fraction. This means, using (9), that

$$\sigma_{As}(\xi) = \sigma_o(T) + \frac{d_o^{\sigma\uparrow} + e_o^{\sigma\uparrow}}{V\varepsilon^{tr}\uparrow} < 0. \tag{15}$$

Note that according to the above conclusions and to the usual approximations for thermoelastic transformations ($e_o^{\sigma\downarrow} = e_1^{\sigma\downarrow} = e_o^\sigma = -e_o^{\sigma\uparrow} = -e_1^{\sigma\uparrow}$) σ_{As} is independent of ξ (and thus of the remaining martensite volume fraction, ξ_r) if one stops the load at a certain deformation, ε_r: $\xi_r \cong \frac{\varepsilon_r}{\varepsilon^{tr}}$, $\varepsilon^{tr\downarrow} = -\varepsilon^{tr\uparrow} = \varepsilon^{tr}$), even in the whole $0 \le \xi \le 1$ interval, since no need for nucleation in the backward process (the existing L-band propagates back). Furthermore, since

$$\sigma_{Ms} = \sigma_o(T) + \frac{d_o^\sigma + e_o^\sigma}{V\varepsilon^{tr}} \tag{16}$$

$$\sigma_{As} = \sigma_o(T) - \frac{d_o^\sigma - e_o^\sigma}{V\varepsilon^{tr}}, \tag{17}$$

the width of the extended (whole) hysteresis loop is $\Delta\sigma \cong \sigma_{Ms} - \sigma_{As} = \frac{2d_o^\sigma}{V\varepsilon^{tr}}$ with $\sigma_{As} < 0$. Thus, the formed martensite is stabilized by the dissipative energy: it has large enough positive value for this. We can give a rough numerical estimate for $\Delta\sigma \cong \sigma_{Ms} - \sigma_{As}$, i.e. for σ_{As}, from the dissipative energy of the closed hysteresis loop, $D_\sigma/V \cong 2d_o^\sigma/V = \Delta\sigma\varepsilon^{tr}$, assuming that the dissipation during normal thermally induced transformation is similar to the one during the L-band propagation, as

$$\sigma_{Ms} - \sigma_{As} = \frac{109}{0.157}\frac{J}{mol} = 694 \quad \frac{J}{mol} = 100MPa.$$

This is expected to be larger than $\sigma_{Ms} \cong$120 MPa, if $\sigma_{As} < 0$, which can fulfil if we assume that the dissipative energy for the stress-strain loop is larger by about 20 % than the one corresponding to the thermal loop.

4.2. Thermal recovery

As it was already described in Section 3.2, the thermally induced martensite to austenite transformation took place in about a 70 K wide temperature interval (Fig. 3). Although it was mentioned in [11] that it is a burst like (explosive) transformation, the large finite width ($A_f - A_s$, the difference of the austenite finish and start temperature), is in odds with other burst like transitions, which typically take place within a few K wide temperature window [44]. In addition, the width of this window is a measure of the slope of the first derivative of the elastic energy, E, stored in the martensite structure [43] (using (5) $A_f - A_s \cong -\frac{e_1 - e_o}{-\Delta s}$, where $e_1 - e_o = -(e_1^{\uparrow} - e_o^{\uparrow}) > 0$). Thus, its small value means that there is no gradual relaxation of the stored elastic energy during heating. In the opposite case, which is observed here, some relaxation of elastic energy takes place. The gradual (stepwise) increase of the cumulative AE energy thus indicates the jerky relaxation of the above elastic energy. The finite width of the thermal recovery means that $-\left(e_1^{T\uparrow} - e_0^{T\uparrow}\right) > 0$, i.e. there is some elastic energy relaxation during thermal recovery and the elastic energy has a quadratic ξ-dependence. The origin of this elastic energy is an interesting question. One of the possible explanation can be that, after removing the stress at the end of stress induced process, some elastic energy can be stored (if after the release of the constrain of the machine heads the elastic strain of the sample is not zero) and heating the free sample this can be relaxed. Another effect can be related to the observation of the presence of the irreversible strain: it increased with increasing transformed martensite volume fraction and it was about 3 % after straining the sample up to about 15 % (Fig. 3b in [11]).

One interesting feature of the width of this thermal recovery should also be noted. It can be seen in Fig. 3b of [11] that the width of the transition gradually decreases with increasing maximum strain and it can be indeed in the order of magnitude of about 10 K (which is already close to typical values for burst like transitions) after the full stress induced transformation. In order to get an explanation for this we can again use the local equilibrium model. For the thermal recovery, after (partial) stress induced martensite formation, we can assume that during the backward propagation of the L-band the dissipative term is the same (the same frictional mechanism) in the whole $0 \le \xi \le 1$ interval (there is no nucleation stage here) as its value for the stress induced process. On the other hand, the elastic term can be different and thus we can write

$$A_s = T_o + \frac{d_o^T + e_1^{T\uparrow}}{-\Delta s} \tag{18}$$

and

$$A_f = T_o + \frac{d_o^T + e_0^{T\uparrow}}{-\Delta s}. \tag{19}$$

For the width of transformation we get

$$A_f - A_s = -\frac{e_1^{T\uparrow} - e_0^{T\uparrow}}{-\Delta s}. \tag{20}$$

For the expression of the dependence of the width on the remaining martensite volume fraction after straining the sample up to about a given ε_r value, $\xi_r = \frac{\varepsilon_r}{\varepsilon^{tr}}$, we can write,

$$\begin{aligned} A_f - A_s(\xi_r) &= -\frac{e_1^{T\uparrow} - e^{T\uparrow}(\xi_r)}{-\Delta s} = -\frac{e_1^{T\uparrow} - e_o^{T\uparrow} - \xi_r\left(e_1^{T\uparrow} - e_o^{T\uparrow}\right)}{-\Delta s} \\ &= \frac{-(e_1^{T\uparrow} - e_o^{T\uparrow})(1 - \xi_r)}{-\Delta s}, \end{aligned} \tag{21}$$

which shows, that the width decreases with increasing remained martensite volume fraction ($-\left(e_1^{T\uparrow} - e_0^{T\uparrow}\right) > 0$) and the width approaches to zero for the pure martensite to austenite transition (burst-like transition), when $\xi_r = 1$.

Similarly, as above the expression for the ξ_r-dependence of the peak temperature one gets

$$\begin{aligned} T_P &= \frac{A_f + A_s(\xi_r)}{2} = T_o + \frac{d_o^T}{-\Delta s} + \frac{e_1^{T\uparrow} + e_o^{T\uparrow} + \xi_r\left(e_1^{T\uparrow} - e_o^{T\uparrow}\right)}{-2\Delta s} \\ &= T_o + \frac{d_o^T}{-\Delta s} + \frac{E^{T\uparrow}}{-\Delta s} + \frac{\left(e_1^{T\uparrow} - e_o^{T\uparrow}\right)(1 - \xi_r)}{-2\Delta s} = T_p(\xi_r = 0) - \frac{\xi_r\left(e_1^{T\uparrow} - e_o^{T\uparrow}\right)}{-2\Delta s} \end{aligned} \tag{22}$$

which predicts that the peak temperature is expected to increase with the remained martensite volume fraction. Although data shown in Fig. 3 of [11] seem to confirm the above conclusions on the width and the peak position, due to the experimental scatter and due to the effect of the residual strain after recovery, further carefully designed and implemented experiments are desirable to get a quantitative agreement.

4.3. *Characteristic exponents*

It can be seen from Table 1 and Table 2 that the characteristic exponents for the Lüders band nucleation and propagation as well as for thermal recovery are the same within the errors bars, thus on the basis of these we can conclude that the AE source mechanisms are the same. This is also supported by the fact that the duration times of the avalanches emitted during stress induced transformation as well as thermal recovery cover practically the same time interval for both cases, since for different mechanisms the duration times of the signals can differ significantly [26].

The values of the exponents can be compared with values obtained from AE investigation of stress induced martensitic transformations and during (burst like) thermal recover in $Ni_{49}Fe_{18}Ga_{27}Co_6$ shape memory single crystals [44] where $\alpha = 2.9 \pm 0.3$ and $\varepsilon = 1.8 \pm 0.1$ as well as $\alpha = 3.0 \pm 0.3$ and $\varepsilon = 1.8 \pm 0.1$ were obtained, respectively. It can be seen that these agree well with data given in Tables 1 and 2.

5. Conclusions

It is shown that the Lüders-type martensite nucleation and propagation are intermittent processes and result in acoustic emission signals. There is large AE activity at the band localization and it gradually decreases during the propagation. The large acoustic activity at the band localization is due to the presence of nucleation barrier of elastic origin proportional to the Lüders-peak area. The propagation of the band is jerky and results in local stress drops, accompanied with emission of AE signals. Sub-cycles of the propagation stage showed AE activity in accordance with the Kaiser effect. The martensite formed during stress loading is stabilized by the large dissipative energy. The gradual stepwise increase of the cumulative AE energy indicates jerky relaxation of elastic energy during thermal recovery. The characteristic exponents of the AE signals obtained during Lüders-type transformation and thermal recovery are the same within the error bars and agree well with data obtained during stress or temperature induced processes in $Ni_{49}Fe_{18}Ga_{27}Co_6$ shape memory single crystals.

CRediT authorship contribution statement

Lajos Daróczi: Writing – review & editing, Validation, Methodology, Investigation, Formal analysis. **Tóth László Z.:** Visualization, Software, Formal analysis, Data curation. **Azim Asmaa A.:** Writing – original draft, Visualization, Investigation, Formal analysis, Data curation. **Beke Dezso L.:** Writing – review & editing, Writing – original draft, Validation, Supervision, Methodology, Conceptualization. **Kireeva Irina V.:** Writing – review & editing, Methodology, Conceptualization. **Chumljakov Yuriy I.:** Writing – review & editing, Project administration, Methodology, Funding acquisition, Conceptualization.

Declaration of Competing Interest

The authors declare the following financial interests/personal relationships which may be considered as potential competing interests Y. I. Chumljakov reports financial support was provided by Ministry of Science and Higher Education of the Russian Federation. Reports a relationship with that includes:. Has patent pending to. If there are other authors, they declare that they have no known competing financial interests or personal relationships that could have appeared to influence the work reported in this paper.

Acknowledgments

This work was supported by the Ministry of Science and Higher Education of the Russian Federation (project No. FSWM-2024–0007).

References

[1] J.A. Shaw, S. Kyriakides, On the nucleation and propagation of phase transformation fronts in a NiTi alloy, Acta Mater. 45 (1977) 673–700, https://doi.org/10.1016/S1359-6454(96)00189-9.

[2] P. Sedmák, J. Pilch, L. Heller, J. Kopeček, J. Wright, P. Sedlák, M. Frost, P. Šittner, Grain-resolved analysis of localized deformation in nickel-titanium wire under tensile load, Science 353 (2016) 559–562, https://doi.org/10.1126/science.aad6700.

[3] M. Peigney, A micromechanically consistent energy estimate for polycrystalline shape-memory alloys, II: Application to Lüders-type strain localization, J. Mech. Phys. Solids 173 (2023) 1052200, https://doi.org/10.1016/j.jmps.2023.105220.

[4] Y. Li, B.S. Shariat, H. Yang, Y. Liu, Influences of extrinsic factors on the Lüders-type deformation behaviour of NiTi, Mater. Sci. Eng. A 862 (2023) 144418, https://doi.org/10.1016/j.msea.2022.144418.

[5] Y. Li, B. Shariat, H. Yang, S. Sarkar, J. Zhang, Y. Wang, D. Favier, Y. Liu, A mechanical criterion for Lüders-type deformation of polycrystalline NiTi, Acta Mater. 245 (2023) 118604, https://doi.org/10.1016/j.actamat.2022.118604.

[6] K.M. Golasiński, M. Maj, W. Tasaki, E.A. Pieczyska, H.Y. Kim, Full-field deformation study of Ti–25Nb, Ti–25Nb–0.3O and Ti–25Nb–0.7O shape memory alloys during tension using digital image correlation, Metall. Mater. Trans. A 55 (2024) 2509–2518, https://doi.org/10.1007/s11661-024-07414-8.

[7] R. Sidharth, Y. Wu, F. Brenne, W. Abuzaid, H. Sehitoglu, Relationship between functional fatigue and structural fatigue of iron-based shape memory alloy FeMnNiAl, Shape Mem. Superelast 6 (2020) 256–272, https://doi.org/10.1007/s40830-020-00283-1.

[8] H. Chen, H. Sun, Y. Ren, J. Yang, C. Song, D. Cong, S. Li, Y.-D. Wang, Achieving near zero-hysteretic superelasticity in a Ni43Fe18Ga27Co12 single-crystalline microwire via Lüders-like phase transformation, Scr. Mater. 242 (2024) 115932, https://doi.org/10.1016/j.scriptamat.2023.115932.

[9] C. Efstathiou, H. Sehitoglu, J. Carroll, J. Lambros, H.J. Maier, Full-field strain evolution during intermartensitic transformations in single-crystal NiFeGa, Acta Mater. 56 (15) (2008) 3791–3799, https://doi.org/10.1016/j.actamat.2008.04.033.

[10] F. Bubani, C. de, M. Sade, F. Lovey, Improvements in the mechanical properties of the 18R↔6R high-hysteresis martensitic transformation by nanoprecipitates in CuZnAl alloys, Mater. Sci. Eng. A 543 (2012) 88–95, https://doi.org/10.1016/j.msea.2012.02.051.

[11] I.V. Kireeva, Y.I. Chumlyakov, A.A. Saraeva, A.V. Vyrodova, Gaint shape memory effect of the $[\bar{1}44]$ oriented FCC CrMnFeCoNi high-entropy alloys single crystals with FCC→HCP martensitic transformation, Scr. Mater. 235 (2023) 115621, https://doi.org/10.1016/j.scriptamat.2023.115621.

[12] B.S. Shariat, Y. Li, H. Yang, Y. Wang, Y. Liu, On the Lüders band formation and propagation in NiTi shape memory alloys, J. Mater. Sci. Technol. 116 (2022) 22–29, https://doi.org/10.1016/j.jmst.2021.11.028.

[13] D.L. Beke, L. Daróczi, L.Z. Tóth, M.K. Bolgár, N.M. Samy, A. Hudák, Acoustic emissions during structural changes in shape memory alloys, Metals 9 (1) (2019) 58, https://doi.org/10.3390/met9010058.

[14] J.F. Hallai, S. Kyriakides, Underlying material response for Lüders-like instabilities, Int. Plast. 47 (2013) 1–12, https://doi.org/10.1016/j.ijplas.2012.12.002.

[15] C.H. Caceres, A.H. Rodriguez, Acoustic emission and deformation bands in Al-2.5Mg and Cu-30Zn, Acta Met. 35 (12) (1987) 2851–2864, https://doi.org/10.1016/0001-6160(87)90284-7.

[16] T.V. Murav'ev, L.B. Zuev, Acoustic emission during the development of a Lüders band in a low-carbon steel, Tech. Phys. 53 (2008) 1094–1098, https://doi.org/10.1134/S1063784208080203.

[17] J. Petit, D. Wagner, N. Ranc, G. Montay, M. François, Comparison of different techniques for the monitoring of the Lüders bands development, Int. Congr. Fract., Beijing, China (2013) hal-01421699.

[18] V.I. Danilov, D.V. Orlova, V.V. Gorbatenko, L.V. Danilova, Effect of temperature on the kinetics of localized plasticity autowaves in Lüders deformation, Metals 13 (2023) 773, https://doi.org/10.3390/met13040773.

[19] W. Zhou, D. Li, Y. Su, et al., Experimental study on the static strain aging of Q345 steel using complementary in-situ non-destructive testing techniques, Int. J. Steel Struct. 24 (2024) 591–606, https://doi.org/10.1007/s13296-024-00840-9.

[20] A. Vinogradov, Signatures of plastic instabilities and strain localization in acoustic emission time-series, Metals 15 (1) (2025) 46, https://doi.org/10.3390/met15010046.

[21] F. Cmelík, F.B. Klose, H. Dierke, J. Šachl, H. Neuhäuser, P. Lukáč, Investigating the Portevin–Le Châtelier effect in strain rate and stress rate controlled tests by the acoustic emission and laser extensometry techniques, Mater. Sci. Eng. A 462 (2007) 53–60, https://doi.org/10.1016/j.msea.2006.01.169.

[22] A. Lazarev, A. Vinogradov, About plastic instabilities in iron and power spectrum of acoustic emission, J. Acoust. Emiss. 27 (2009) 144–156.

[23] M. Janeček, R. Král, P. Dobroň, F. Chmelík, V. Šupík, F. Holländer, Mechanisms of plastic deformation in AZ31 magnesium alloy investigated by acoustic emission and transmission electron microscopy, Mater. Sci. Eng. A 462 (1–2) (2007) 311–315, https://doi.org/10.1016/j.msea.2006.01.172.

[24] E.A. Pieczyska, H. Tobushi, K. Takeda, D. Sts róz, Z. Ranachowski, K. Kulasinski, S. Kuleda Jr, J. Luckner, Martensite transformation bands studied in TiNi shape memory alloy by infrared and acoustic emission techniques, Kov. Mater. 50 (2012) 309–318, https://doi.org/10.4149/km_2012_5_309.

[25] G.F. Nataf, M. Romanini, E. Vives, B. Zuzek, A. Planes, J. Tusek, X. Moya, Suppression of acoustic emission during superelastic tensile cycling of polycrystalline $N_{50.4}Ti_{49.6}$, Phys. Rev. Mater. 4 (2020) 093604, https://doi.org/10.1103/PhysRevMaterials.4.093604.

[26] Y. Chen, B. Gou, B. Yuan, X. Ding, J. Sun, E.K.H. Salje, Multiple avalanche processes in acoustic emission spectroscopy: multibranching of the energy-amplitude scaling, Phys. Status Solidi B 259 (2021) 2100465, https://doi.org/10.1002/pssb.202100465.

[27] Firstov, G.S., Kosurukova, T.A., Koval, Yu.N., & Odnosum, V.V., (2015). High entropy shape memory alloys, Mat. Today: Proceedings 2(S3), S499-S504. https://doi.org/10.1016/j.mtpr.2015.07.335.

[28] J.I. Lee, K. Tsuchiya, W. Tasaki, H.S. Oh, T. Sawaguchi, H. Murakami, T. Hiroto, Y. Matsushita, E.S. Park, A strategy of deigning high entropy alloys with high-temperature shape memory effect, Sci. Rep. 9 (2019) 13140, https://doi.org/10.1038/s41598-019-49529-8.

[29] G. Fu, X. Liu, X. Yi, S. Zhang, X. Cao, X. Meng, Z. Gao, H. Wang, Development of High-entropy shape-memory alloys: a review, Metals 13 (2023) 1279, https://doi.org/10.3390/met13071279.

[30] E. Bronstein, L.Z. Tóth, L. Daróczi, D.L. Beke, R. Talmon, D. Shilo, Tracking twin boundary jerky motion at nanometer and microsecond scales, Adv. Funct. Mater. 31 (2021) 2106573, https://doi.org/10.1002/adfm.202106573.

[31] D.L. Beke, L. Daróczi, L.Z. Tóth, M.K. Bolgár, N.M. Samy, A. Hudák, Acoustic emissions during structural changes in shape memory alloys, Metals 9 (1) (2019) 58, https://doi.org/10.3390/met9010058.

[32] J.P. Setna, K.A. Dahmen, C.R. Myers, Crackling noise, Nature 410 (2001) 242–250, https://doi.org/10.1038/35065675.

[33] M.C. Kuntz, J.P. Setna, Noise in disordered systems: the power spectrum and dynamic exponents in avalanche models, Phys. Rev. B 62 (2000) 11699, https://doi.org/10.1103/PhysRevB.62.11699.

[34] M. LeBlanc, L. Angheluta, K. Dahmen, N. Goldenfeld, Universal fluctuations and extreme statistics of avalanches near the depinning transition, Phys. Rev. E 87 (2013) 022126, https://doi.org/10.1103/PhysRevE.87.022126.

[35] S. Papanikolaou, F. Bohn, R.L. Sommer, G. Durin, S.S. Zapperi, J.P. Setna, Universality beyond power laws and the average avalanche shape, Nat. Phys. 7 (2011) 316–320, https://doi.org/10.1038/nphys1884.

[36] L. Laurson, X. Illa, S. Santucci, K.T. Tallakstad, K.J. Maloy, M.J. Alava, Evolution of the average avalanche shape with the universality class, Nat. Commun. 4 (2013) 2927, https://doi.org/10.1038/ncomms3927.

[37] S.M. Kamel, N.M. Samy, L.Z. Tóth, L. Daróczi, D.L. Beke, Denouement of the energy-amplitude and size-amplitude enigma for acoustic-emission investigations of materials, Materials 15 (2022) 4556, https://doi.org/10.3390/ma15134556.

[38] A. Clauset, C.R. Shalizi, M.E. Newman, Power-law distributions in empirical data, SIAM Rev. 51 (2009) 661–703. ⟨http://www.jstor.org/stable/25662336⟩.

[39] B. Casals, K.A. Dahmen, B. Gou, S. Rooke, E.K.H. Salje, The duration-energy-size enigma for acoustic emission, Sci. Rep. 11 (2021) 5590, https://doi.org/10.1038/s41598-021-84688-7.

[40] F. Chmelík, A. Ziegenbein, H. Neuhäuser, P. Lukáč, Investigating the Portevin–Le Chatelier effect by the acoustic emission and laser extensometry techniques, Mater. Sci. Eng. A 327 (2002) 200–207, https://doi.org/10.1016/S0921-5093(01)01312-0.

[41] H.M. Tensi, The Kaiser-effect and its scientific background, J. Acoust. Emiss. 22 (2004) S1–S16.

[42] Y. Liu, Thermodynamics of the shape memory effect in Ti–Ni alloys, in: T. Yoneyama, S. Miyazaki (Eds.), Shape memory alloys for biomedical applications, Woodhead Publishing Limited, Abington Hall, Granta Park Great Abington, Cambridge CB21 6AH, England, 2009, p. 37, https://doi.org/10.1533/9781845695248.1.37.

[43] D.L. Beke, L. Daróczi, N.M. Samy, L.Z. Tóth, M.K. Bolgár, On the thermodynamic analysis of martensite stabilization treatments, Acta Mater. 200 (2020) 490–501, https://doi.org/10.1016/j.actamat.2020.09.026.

[44] S.M. Kamel, L. Daróczi, L.Z. Tóth, E.Y. Panchenko, Y.I. Chumlyakov, N.M. Samy, D. L. Beke, Acoustic emission and DSC investigations of anomalous stress-stain curves and burst like shape recovery of Ni49Fe18Ga27Co6 shape memory single crystals, Intermetallics 159 (2023) 107932, https://doi.org/10.1016/j.intermet.2023.107932.